GEM NEWS INTERNATIONAL

Contributing Editors
Gagan Choudhary, *IIGJ-Research & Laboratories Centre, Jaipur, India* (gagan.choudhary@iigjrlc.org)
Guanghai Shi, *School of Gemmology, China University of Geosciences, Beijing* (shigh@cugb.edu.cn)

COLORED STONES AND ORGANIC MATERIALS

***Palaeoclavaria burmitis* inclusions in Burmese amber.** Biological inclusions represent an extraordinary and scientifically valuable aspect of amber. Beyond an aesthetic and commercial appeal, these inclusions provide significant insights into ancient ecosystems. Among global amber sources, Burmese amber is particularly renowned for its abundance and diversity of biological inclusions. These inclusions encompass a wide range of organisms, including fauna (ants, bees, beetles, scorpions, lizards, small birds, and snails), flora (leaves, bark, and stems), and fungi.

Recently, during a visit to the Mandalay Gem Market in Myanmar, the authors encountered several high-quality amber specimens containing fossilized fungi and acquired two amber cabochons weighing 131.85 and 130.37 ct and measuring 59.04–39.91 × 21.97 mm and 53.73–40.35 × 21.08 mm, respectively (figure 1). Both specimens displayed a transparent yellow-orange bodycolor.

Standard gemological testing revealed specific gravity values of 1.05 and 1.04, with a spot refractive index of 1.50 for both. Neither sample reacted with acetone. Fourier-transform infrared (FTIR) spectroscopy exhibited characteristic absorption peaks at approximately 2923, 2852, 1720, 1450, 1150, 1030, and 813 cm^{-1}, with the notable absence of the 887 cm^{-1} peak typical of copal. These findings confirmed that the specimens were natural amber, exhibiting diagnostic features consistent with Burmese amber (L.N. Nang et al., "Characteristics of newly discovered amber from Phu Quoc, Vietnam," Summer 2022 *G&G*, pp. 184–194). Each piece contained a cluster of approximately 20–25 fungal fruiting bodies. Based on morphological characteristics, these inclusions were identified as *Palaeoclavaria burmitis*—an extinct fungal species observed only in Burmese amber (G.O. Poinar and A.E. Brown, "A non-gilled hymenomycete in Cretaceous amber," *Mycological Research*, Vol. 107, No. 6, 2003, pp. 763–768) (figure 2, left).

Figure 1. Two amber specimens (131.85 and 130.37 ct, respectively) containing Palaeoclavaria burmitis *fungal inclusions. Photo by Ta Quan Ngoc.*

Editors' note: Interested contributors should send information and illustrations to gandgeditorial@gia.edu.

Gems & Gemology, Vol. 61, No. 3, pp. 316–330.

Within the amber, the *Palaeoclavaria burmitis* inclusions were preserved with a granular gray outer surface and an interior ranging in color from light gray to black (figure 2, right). The fruiting bodies measured ~1–3 mm in diameter and reached heights of ~2–4 mm. Notably, nearly colorless siliceous crystalline structures were observed within the fungal tissues—a diagnostic feature indicative of fossilization through silicification replacement. These

Figure 2. Left: Lateral view of Palaeoclavaria burmitis *fungal inclusions in the 131.85 ct Burmese amber sample. Right: Cross section of the* Palaeoclavaria burmitis *inclusions showing a siliceous crystalline structure. Photos by Le Ngoc Nang; field of view 4 mm (right).*

crystalline clusters exhibited a higher degree of crystallinity than the surrounding material, forming microcrystalline quartz or chalcedony—types of silica crystallization commonly found in siliceous fossils as well as in silica precipitates from magmatic sources (especially within chalcedony masses).

FTIR spectroscopy of the fungal interior confirmed the presence of silica, indicated by absorption peaks at 1006, 775, and 693 cm^{-1} (B.C. Smith, "Inorganics III: Even more spectra, and the grand finale," *Spectroscopy*, Vol. 39. No. 3, 2024, pp. 11–15), along with organic compound bands at 1431 and 1625 cm^{-1} and water at a peak of 3622 cm^{-1} (figure 3) (R.H. Ellerbrock and H.H. Gerke, "FTIR spectral band shifts explained by OM–cation interactions," *Journal of Plant Nutrition and Soil Science*, Vol. 184, No. 3, 2021, pp. 388–397). These data suggest that the fungi underwent siliceous replacement fossilization—a separate process from the surrounding amber's polymerization.

Figure 3. FTIR spectrum confirming the presence of siliceous material, along with organic compounds and water.

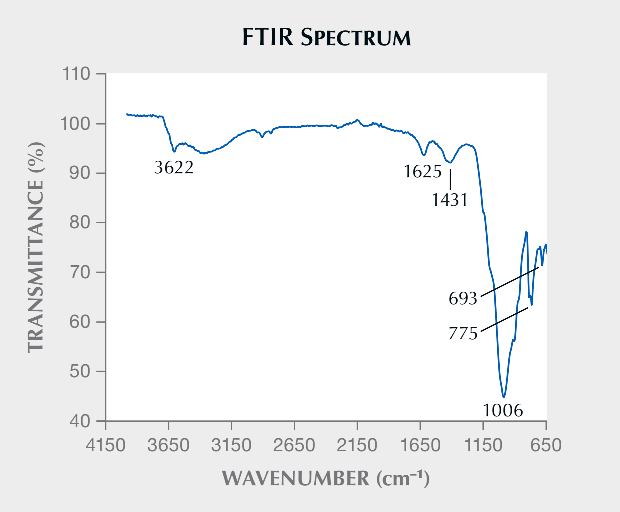

Fungi belong to a unique biological kingdom, distinct from both plants and animals, and are rarely fossilized outside of the amber environment. According to a comprehensive study by Poinar Jr. (G. Poinar Jr., "Fossil fleshy fungi ('mushrooms') in amber," *Fungal Genomics & Biology*, Vol. 6, No. 2, 2016, article no. 1000142), each amber deposit contains a unique assemblage of fungal taxa. Fungi identified in Dominican amber include *Aureofungus yaniguaensis*, *Protomycena electra*, *Coprinites dominicana*, *Favolaschia* sp., *Xylaria antiqua*, *Ganoderma* sp., and *Paleomorchella dominicana* sp. nov.; *Gerontomyces lepidotus* in Baltic amber; and *Palaeoagaracites antiquus*, *Palaeogaster micromorpha*, and *Palaeoclavaria burmitis* in Burmese amber. These fungal taxa differ markedly in geological age, geographic distribution, and morphology. As such, they serve as reliable paleobiological markers for determining the provenance and geological age of amber specimens with high accuracy.

Le Ngoc Nang
Liu Gemological Research and Application Center
Ho Chi Minh City, Vietnam

Ta Quan Ngoc
Bong Cam Thach Myanmar
Ho Chi Minh City, Vietnam

Trapiche pattern formation of grossular garnets. The six-fold rotational symmetric pattern, called trapiche, is commonly reported in hexagonal or trigonal crystal system minerals such as beryl, corundum, tourmaline, and quartz, but also can be found in diamond, spinel, and garnet having a cubic crystal system (J. Bergman, "Trapiche: The rising star," *InColor*, No. 31, 2016, pp. 32–44). Recently, three near-colorless transparent tablets with six-rayed black inclusions arranged in a snowflake-like pattern forming a trapiche structure were submitted to GIA's Tokyo laboratory for identification (figure 4A). Standard gemological properties, Raman spectra, and chemical analyses using energy-dispersive X-ray fluorescence identified the stones as grossular garnets, composed mainly of $Ca_3Al_2Si_3O_{12}$. The arms and cores were black due to irregular black inclusions, and the samples also contained numerous colorless transparent inclusions (figure 4B). In cross-polarized light, the largest stone, weighing 1.00 ct, showed a clear concentric hexagonal light and dark pattern (figure 4C). The three submitted samples were very similar to the recently reported trapiche grossular garnets from Zhejiang Province, China (Y. Wang et al., "Trapiche garnets in Chun'an, Zhejiang Province, China: New constraints from their gemology, geochemistry, and geochronology," *Crystals*, Vol. 15, No. 3, 2025, article no. 201; T. Hainschwang, "Trapiche grossular from China," *Journal of Gemmology*, Vol. 39, No. 5, 2025, pp. 418–421; Summer 2025 GNI, pp. 208–210).

Typical idiomorphism of single crystal gemstones, such as hexagonal prismatic emeralds, octahedral diamonds, and rhombic dodecahedral garnets, is the thermodynamic equilibrium shape in which the sum of all surface energies is minimized (Wulff's theorem). Since the distance between the euhedral facets and the center is shorter than that between the apexes and the center, it is clear that the euhedral facets grow slower than the apexes. This slower crystal growth for the flat euhedral facets as compared to the apexes relates to the fact that they are smooth at the atomic level and have fewer defects (e.g., Y. Saito, *Statistical Physics of Crystal Growth*, World Scientific, Singapore, 1996). A smooth surface is one in which the constituent atoms in a crystal structure (i.e., the lattice points that represent molecular groups) are most densely packed. The densest plane can be determined primarily by the mineral's Bravais lattice type. The seven crystal systems are further classified into 14 types of Bravais lattices by considering four unit cell lattice patterns: primitive, body-centered, face-centered, and base-centered. Snowflakes and emeralds (beryls) have primitive hexagonal lattices, diamonds have face-centered cubic (fcc) lattices, and garnets have body-centered cubic (bcc) lattices (figure 5, first column). A primitive hexagonal lattice often forms a hexagonal prism or plate consisting of two basal pinacoids {0001} and six prism faces $\{10\bar{1}0\}$. An fcc lattice has the {111} plane where the lattice points are densest and often forms a euhedral octahedron. On the other hand, the densest plane for a bcc lattice is the {110} and often forms a euhedral rhombic dodecahedron (Bravais' empirical law; figure 5, second column).

The critical nuclei, which are the earliest stages of crystal growth and are the smallest crystals nucleated, have the shapes of small equilibrium euhedral crystals that depend on the Bravais lattices (figure 5, third column; e.g., Saito, 1996). Immediately after the critical nuclei are formed, or after a certain amount of growth, if the driving force for growth (such as supersaturation of gemstone components in the magma or fluid) increases, the gems will grow rapidly.

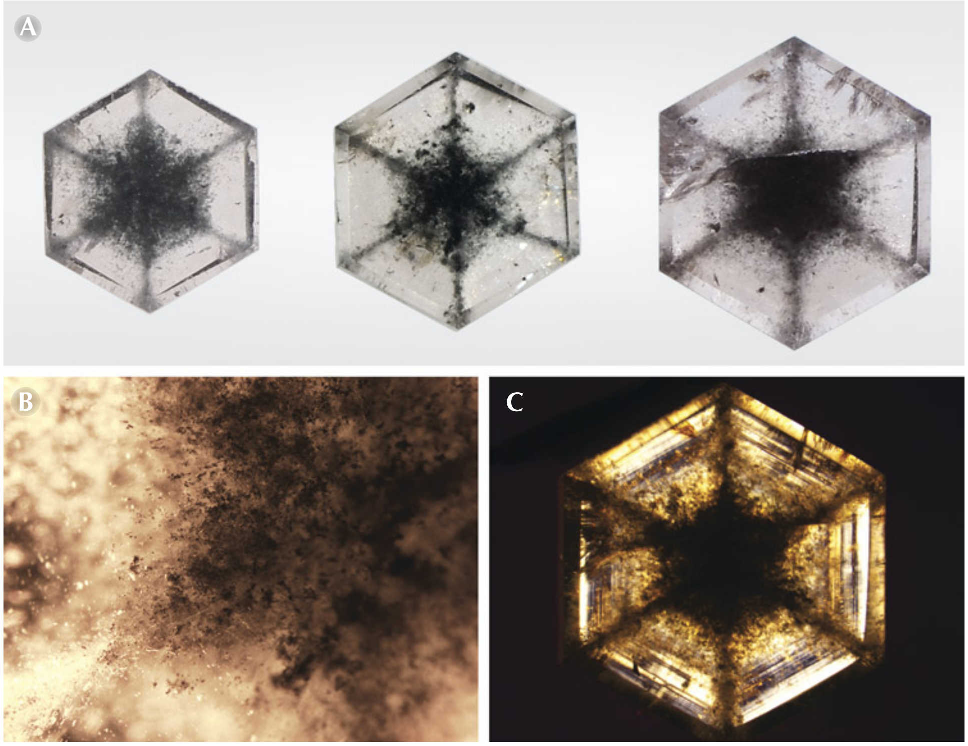

Figure 4. A: Three near-colorless transparent grossular garnet tablets with black inclusions arranged in snowflake-like patterns: 0.46, 0.68, and 1.00 ct, respectively. B: Black and colorless inclusions in the 0.46 ct sample; field of view 1.10 mm. C: Concentric hexagonal light and dark growth pattern of the 1.00 ct stone in cross-polarized light. Photos by Shunsuke Nagai (A) and Taku Okada (B and C).

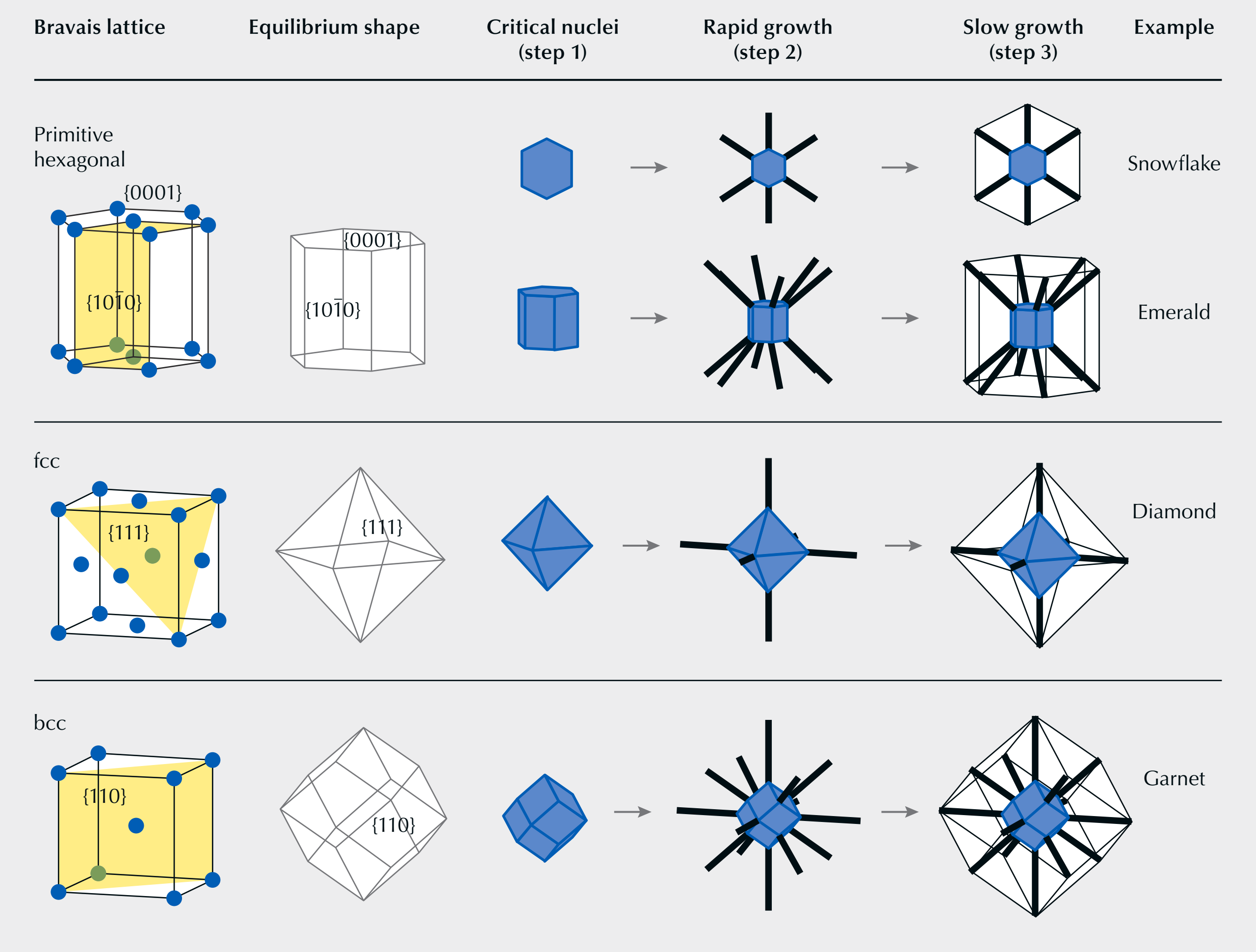

Figure 5. According to Bravais' empirical law, a primitive hexagonal lattice forms a hexagonal prism, a face-centered cubic (fcc) lattice forms an octahedron, and a body-centered cubic (bcc) lattice forms a rhombic dodecahedron as an equilibrium euhedral shape, respectively (modified from M. Tachibana, Beginner's Guide to Flux Crystal Growth, *NIMS Monographs, Springer, Tokyo, 2017). The shape of the critical nuclei corresponds to the equilibrium euhedral shape. In rapid growth, the sharpest corners of the euhedral crystal grow preferentially along the extension of each axial diagonal. Note that the size of the euhedral core crystal may or may not be observable. In slow growth, equilibrium euhedral shapes are again formed as the external shapes.*

In general, the sharpest corners of a euhedral crystal will preferentially grow faster due to the greater supersaturation as well as the "rough" interface (figure 5, fourth column). At this time, the tiny inclusions suspended in the magma or fluid will not be expelled from the gems and will instead be trapped inside and solidified. In fact, Monte Carlo simulations showed that branched dendritic crystals formed in the early stages of garnet growth when the gem's component was highly supersaturated in fluid (D.E. Wilbur and J.J. Ague, "Chemical disequilibrium during garnet growth: Monte Carlo simulations of natural crystal morphologies," *Geology*, Vol. 34, No. 8, 2006, pp. 689–692). These Monte Carlo simulations explain processes that are also reflected in the growth processes and shapes of snowflakes (e.g., K.G. Libbrecht, *Snow Crystals: A Case Study in Spontaneous Structure Formation*, Princeton University Press, Princeton, New Jersey, 2022).

Trapiche emerald and garnet and stellate diamond crystals seem to rapidly grow into a dendritic shape, incorporating the surrounding impurities into six axial diagonals consisting of the 12 vertices of a hexagonal prism in the case of emerald, three axial diagonals consisting of the six vertices of an octahedron in the case of diamond, and seven axial diagonals consisting of the 14 vertices of a rhombic dodecahedron in the case of garnet (figure 5, fourth column). During this rapid growth phase, the fastest growth is along the sector boundaries (the axial diagonals), forming a 3D internal structure such as the six axial diagonal black lines seen in the rough trapiche emeralds reported by Schmetzer (Spring 2019 GNI, pp. 156–158). Alternatively, axial thickening may occur, incorporating impurities, as seen in diamond, where six thick "hydrogen clouds" are separated by a central core (Summer 2024 Lab Notes, pp. 212–214). Then, when the growth rate slows down due to a decrease in supersaturation or a change in temperature or pressure, the crystal approaches equilibrium with the surrounding environment, and the densest faces grow slowly, forming an equilibrium euhedral crystal again (figure 5, fifth column). These growth processes correspond to the formation of a central core by slow growth on a smooth surface (step 1), the formation of a skeleton structure by fast adhesive growth on a rough interface (step 2), and the formation of an outer shape by slow growth on a smooth surface (step 3) as the driving force for growth changes (I. Sunagawa et al., "Texture formation and element partitioning in trapiche ruby," *Journal of Crystal Growth*, Vol. 206, No. 4, 1999, pp. 322–330; I. Pignatelli et al., "The texture and chemical composition of trapiche ruby from Khoan Thong, Luc Yen mining district, Northern Vietnam," *Journal of Gemmology*, Vol. 36, No. 8, 2019, pp. 726–746).

We do not know how the submitted trapiche tablets were physically sliced from the euhedral crystals, but our observations and growth model indicate that they were sliced along the {111} planes (figure 6), and are central portions of garnet single crystals in which black inclusions have been distributed along the seven axial diagonals of a rhombic dodecahedron. Our model differs from the reporting in Wang et al. (2025), but is consistent with the latest detailed report in Wu et al. (Summer 2025 GNI, pp. 208–210). In the case of an octahedral diamond with an fcc lattice, the hydrogen clouds included along the three <100> axes connecting the rapidly growing vertices appear as four lines when viewed along the <100> axis but six lines when viewed along the <111> axis (e.g., W. Wang and W. Mayerson, "Symmetrical clouds in diamond – The hydrogen connection," *Journal of Gemmology*, Vol. 28, No. 3, 2002, pp. 143–152). Since the "essential symmetry" of the cubic crystal system is four three-fold axes of symmetry along four equivalent <111> axes, the six-rayed "star" or trapiche pattern seen in such cubic gemstones is a pseudo six-fold rotational symmetry observable only through inclusions produced by three-fold rotation-inversion symmetry. By conducting thought experiments based on crystallography and crystal growth theory to study the trapiche pattern formation process in garnets exhibiting the complicated euhedral rhombic dodecahedron, to our knowledge we have explained the apparent six-fold symmetry that can appear in cubic gemstones and established a growth model that can be applied to trapiche pattern formation in gems of various crystal systems and Bravais lattice types.

Taku Okada and Kazuko Saruwatari
GIA, Tokyo

Figure 6. The seven axial diagonals in a rhombic dodecahedron viewed from different angles. Left: The blue lines are the three equivalent <100> axes, and the red lines are the four equivalent <111> axes. Center: Cutting along the two yellow dotted lines perpendicular to a <111> axis gives a uniform regular hexagonal plate. Right: The black snowflake-like pattern in trapiche garnets corresponds to three equivalent <111> axes (red lines) excluding the central <111> axis. Three equivalent <100> axes (blue lines) intersecting at higher angles may produce the black core.

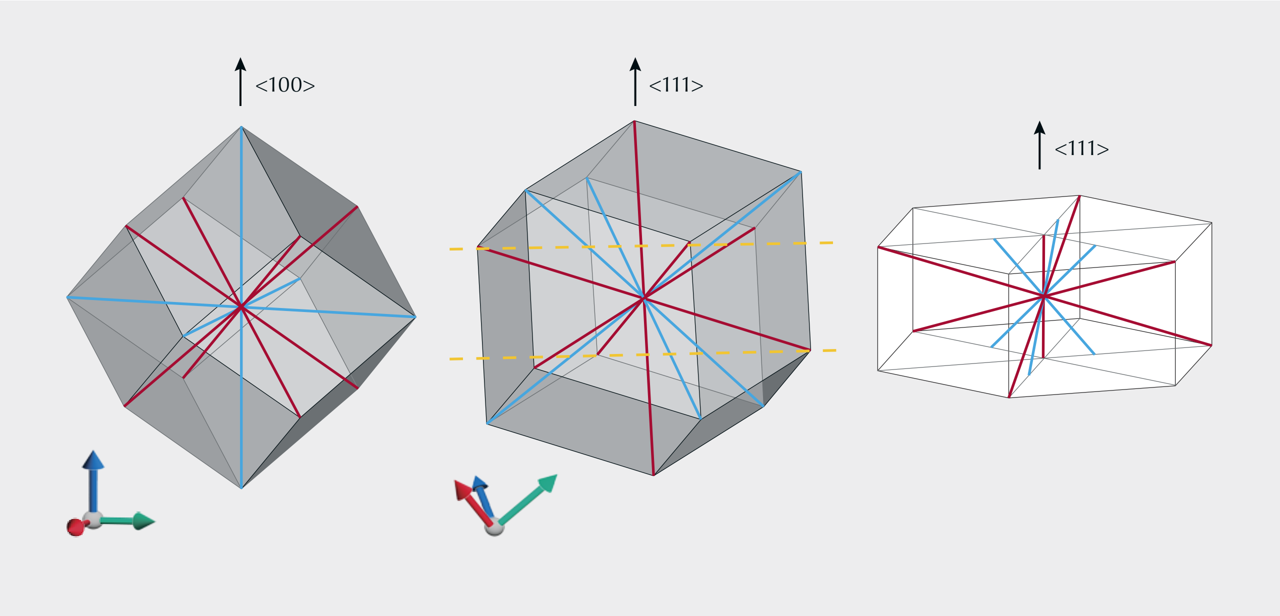

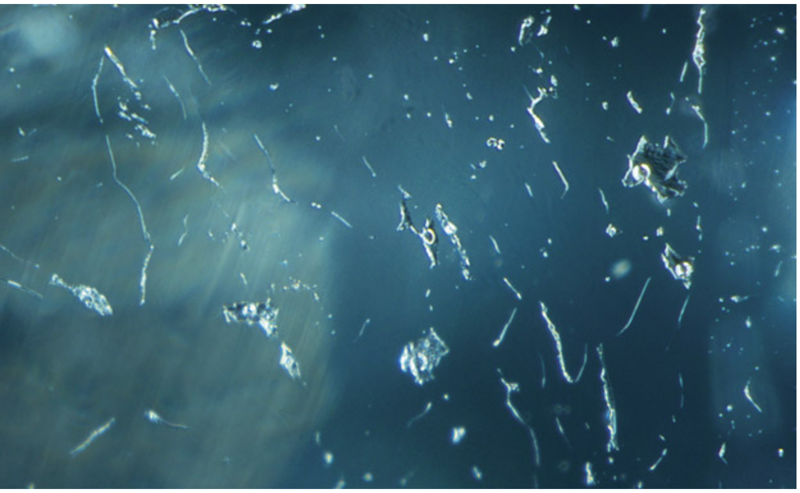

Figure 7. Immiscible two-phase fluid inclusions in a 0.48 ct Paraíba tourmaline. All circular phases were identified as gaseous CO_2 by confocal Raman spectroscopy. Photomicrograph by Kazuko Saruwatari; field of view 1.10 mm.

Gaseous carbon dioxide phases in Paraíba tourmaline. Recently, the authors encountered immiscible two-phase fluid inclusions in several Paraíba tourmaline stones. One stone weighed 0.48 ct and contained many two-phase inclusions (figure 7). Confocal Raman spectroscopy using a 100× objective lens detected carbon dioxide peaks of various intensities at around 1285 and 1388 cm^{-1} in the circular phases, identifying them as gaseous CO_2 (L. Li et al., "In situ Raman spectral characteristics of carbon dioxide in a deep-sea simulator of extreme environments reaching 300°C and 30MPa," *Applied Spectroscopy*, Vol. 72, No. 1, 2017, pp. 48–59) (figure 8), while no specific peaks were observed in the matrix phases. The most likely candidate for the matrix phase was liquid water (H_2O; e.g., H. Beurlen et al., "Geochemical and geological controls on the genesis of gem-quality 'Paraíba tourmaline' in granitic pegmatites from northeastern Brazil," *Canadian Mineralogist*, Vol. 49, No. 1, 2011, pp. 277–300), but it was difficult to detect because the Raman modes of O-H in tourmaline overlap with the two main O-H stretching modes at 3657 and 3756 cm^{-1} of liquid H_2O (M.L. Frezzotti et al., "Raman spectroscopy for fluid inclusion analysis," *Journal of Geochemical Exploration*, Vol. 112, 2012, pp. 1–20).

It is generally known that natural H_2O-CO_2 fluid inclusions can collapse when heated to approximately 350°C (R.J. Bodnar, "Introduction to aqueous-electrolyte fluid systems," in I. Samson et al., *Fluid Inclusions: Analysis and Interpretation*, Mineralogical Association of Canada, Short Courses Vol. 32, 2003, pp. 81–99), which is lower than the conventional heating temperature of Paraíba tourmaline (Spring 1990 Gem News, p. 103). The immiscible coexistence of small amounts of gaseous CO_2 and possible liquid H_2O phases, and the absence of many tension fissures, may be evidence that the Paraíba tourmaline did not undergo heat treatment. To verify this, further heating experiments are needed.

Kazuko Saruwatari and Taku Okada

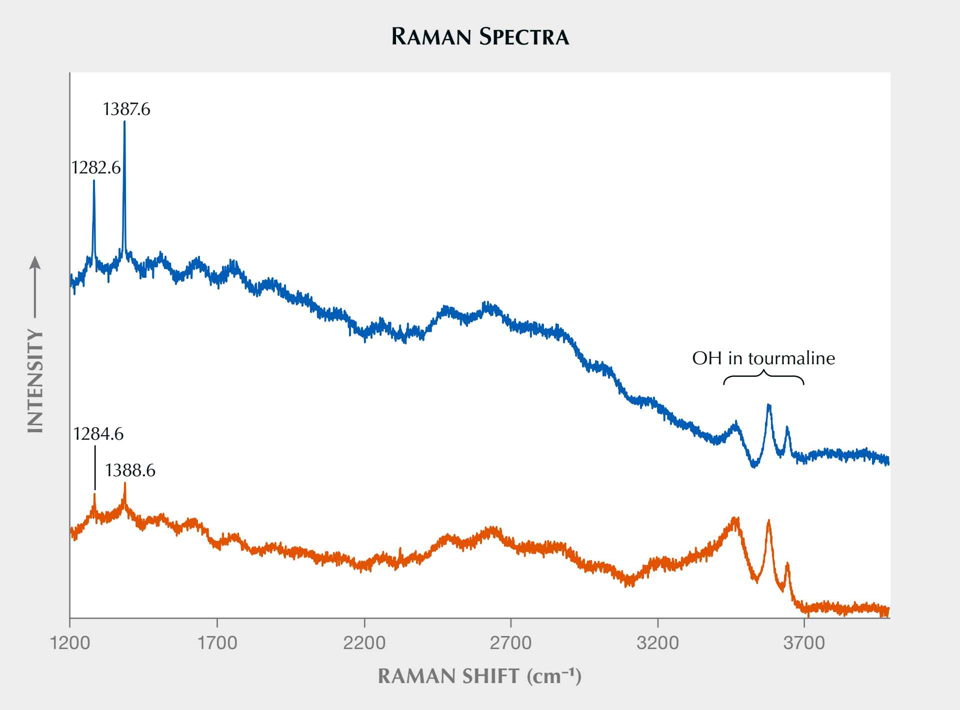

Figure 8. Raman spectra of two gas phases shown in figure 7. The upper Raman spectrum displays stronger CO_2 fermi doublets at 1282.6 and 1387.6 cm^{-1}, while the lower Raman spectrum shows weaker CO_2 fermi doublets at 1284.6 and 1388.6 cm^{-1}. The three broad peaks between 3200 and 3700 cm^{-1} are hydroxyl (OH) peaks of the tourmaline host. Spectra are offset vertically for clarity.

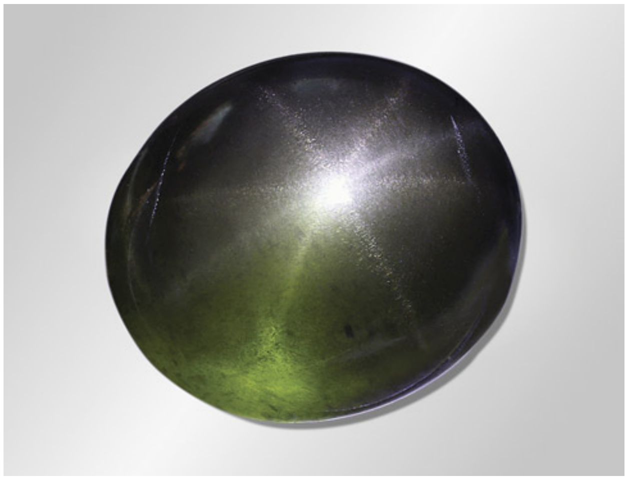

Figure 9. Eight-rayed star peridot from Myanmar weighing 34.16 ct. Photo by Karola Sieber.

Large peridot from Myanmar with an eight-rayed star. Peridot is the gemstone variety of the mineral olivine, a solid solution series with the end members forsterite (Mg_2SiO_4) and fayalite (Fe_2SiO_4). Peridot crystallizes in the orthorhombic system. Its main commercial sources include the Mogok region in Myanmar, the San Carlos area in the U.S. state of Arizona, and, more recently, the Yanbian Chaoxianzu area in China's Jilin Province.

Star peridot is rare and mostly occurs with a four-rayed star (L.B. Benson, Jr., "Highlights at the Gem Trade Lab in Los Angeles," Spring 1960 *G&G*, p. 3), though extremely rare six-rayed (R.T. Liddicoat, Jr., "Highlights at the Gem Trade Lab in Los Angeles: Rare star peridot," Spring 1970 *G&G*, p. 150) and eight-rayed (M.P. Steinbach, *Asterism: Gems with a Star*, MPS Publishing and Media, 2016; M.P. Steinbach, *Star Gems: A Fascinating World*, MPS Publishing and Media, 2023) star peridots have been identified. In the case of the apparent eight-rayed star, it was proposed that the phenomenon was caused by diasterism, in which the star is viewed in transmitted light.

Figure 10. Short reflective needles create one of the four-rayed stars in the eight-rayed star peridot. Photomicrograph by Liviano Soprani; field of view 3 mm.

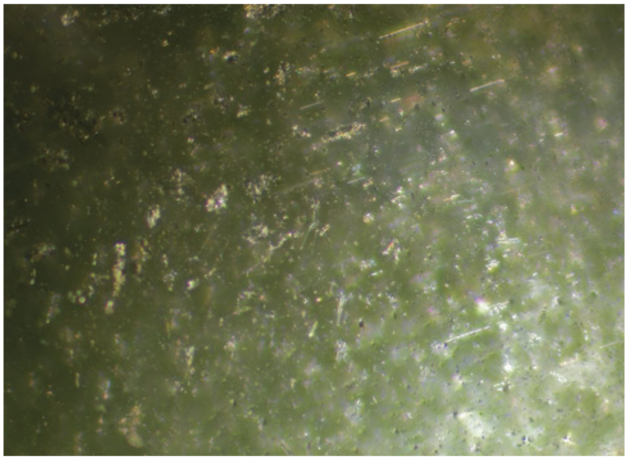

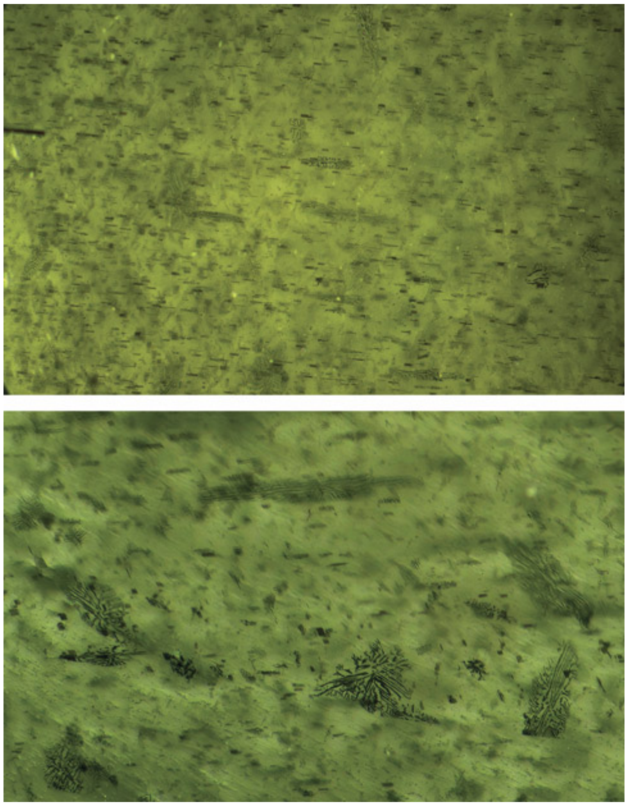

Figure 11. Top: Dark short needles and elongated particle clouds are responsible for the second four-rayed star, oriented at a 45-degree angle to the first star. Bottom: Skeletal inclusions, likely of dissolved magnetite. Photomicrographs by Liviano Soprani; fields of view 2.5 mm (top) and 2.0 mm (bottom).

During the 2023 Hong Kong Gem and Jewellery Fair, author MPS purchased an eight-rayed star peridot reportedly from Myanmar weighing 34.16 ct (figure 9). The oval cabochon measured 17.61 × 15.48 × 13.82 mm and exhibited eye-visible dark inclusions. The stone was identified as peridot by Raman spectroscopy. Compared to the eight-rayed star mentioned above (examined in transmitted light), this star was readily visible in reflected light, a phenomenon called epiasterism. To our knowledge, eight-rayed star peridots exhibiting epiasterism have not been previously described.

Microscopic analysis revealed two sets of inclusions, each creating a four-rayed star oriented 45-degrees apart, forming an eight-rayed star. The first set consisted of short light-colored reflective needles (figure 10) (see Spring 2020 GNI, pp. 159–160). The second set was comprised of thicker black acicular inclusions and elongated clouds of dark particles (figure 11, top). Such needles and dendritic inclusions were previously described in a four-rayed star peridot from Myanmar and identified as magnetite by Raman spectroscopy (Fall 2020 Lab Notes, pp. 422–423). Several of these inclusions were observed in this studied stone as well and are most likely skeletal magnetite (figure 11, bottom).

The eight-rayed star, made up of light- and dark-colored needle-like inclusions, resembles a combination of the four-rayed stars observed in two smaller stones studied for comparison (figure 12). A 2.89 ct lighter colored star peridot with sharp reflective needles and a 3.56 ct darker colored star peridot with dark cloud-like particles showed nearly identical inclusions to those described in the eight-rayed sample, and the colors of the stones are similar.

To the authors' knowledge, an eight-rayed star peridot with a star system made up of two different sets of inclusions has not been described before, and the authors feel privileged to report on this rarity.

Martin P. Steinbach
Steinbach–Gems with a Star
Idar-Oberstein, Germany

Lore Kiefert
Gemmology Consulting
Heidelberg, Germany

Jeanette Fiedler
Deutsches Diamant Institut
Pforzheim, Germany

Figure 12. Similar inclusions observed in a 2.89 ct lighter colored four-rayed star peridot (top) and a 3.56 ct darker colored four-rayed star peridot (bottom) studied for comparison. Photomicrographs by Lore Kiefert; fields of view approximately 2.0 mm (top) and 1.8 mm (bottom).

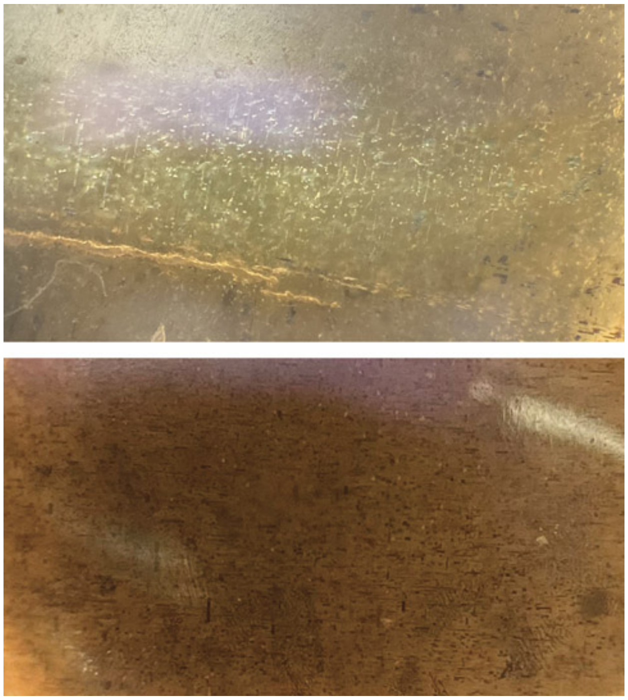

Blue color in quartz caused by elbaite inclusions. Blue color in quartz is usually caused by micro-inclusions of dumortierite (Spring 2015 GNI, pp. 100–102). Although other blue minerals, such as chrysocolla, apatite, and chlorapatite, have been reported as inclusions in quartz, they have not been known to impart a blue bodycolor to quartz (Spring 2015 GNI, pp. 89–90; Summer 2017 *G&G* Micro-World, pp. 241–242; Spring 2022 *G&G* Micro-World, p. 62).

Recently, three semitransparent to opaque quartz spheres weighing 4.85, 5.40, and 5.50 ct, and measuring 9.04, 9.26, and 9.28 mm in diameter, respectively (figure 13, top), were submitted for identification to the National Gemstone Testing Center (NGTC) in Shenzhen, China. Under fiber-optic transmitted illumination, the specimens each exhibited a blue color associated with numerous needle-like blue inclusions.

The spot refractive index of the specimens was approximately 1.55, while hydrostatically calculated specific gravity (SG) values spanned from 2.50 to 2.65. Standard

Figure 13. Top: Three quartz spheres weighing 4.85, 5.50, and 5.40 ct, respectively, colored by blue needle-like inclusions. Bottom: Abundant needle-like blue mineral inclusions in the 5.50 ct quartz sphere, with some displaying triangular cross sections; field of view 1.75 mm. Photos by Rong Liang.

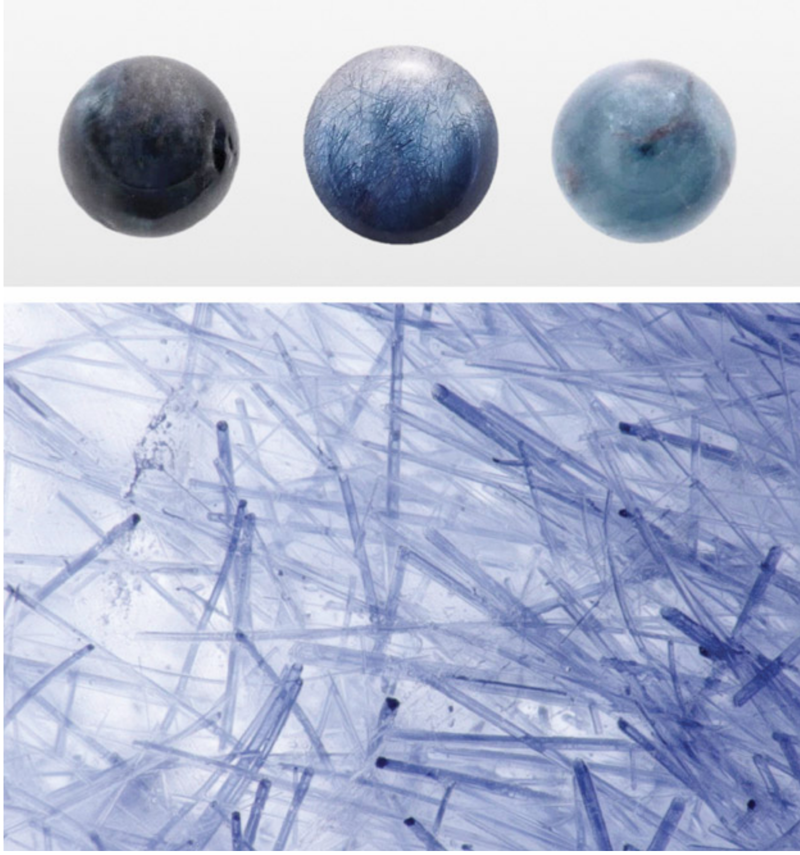

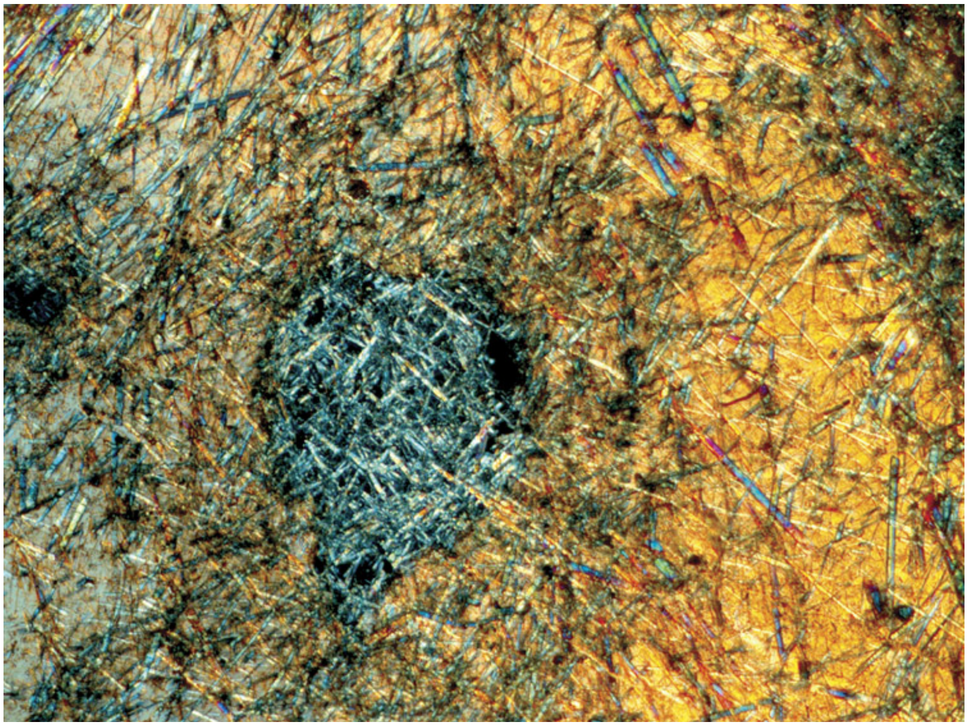

Figure 14. Under cross-polarized light, numerous prismatic inclusions are distributed within the 4.85 ct sphere. Photomicrograph by Rong Liang; field of view 2.15 mm.

gemological testing, along with Fourier-transform infrared (FTIR) spectroscopy, identified the host material as quartz. Microscopic examination revealed abundant needle-like mineral inclusions and healed fractures. These inclusions were either clustered or randomly distributed, with some displaying a triangular cross-sectional morphology (figure 13, bottom). The samples' surfaces showed resin-impregnated fractures contrasting with the inherent vitreous

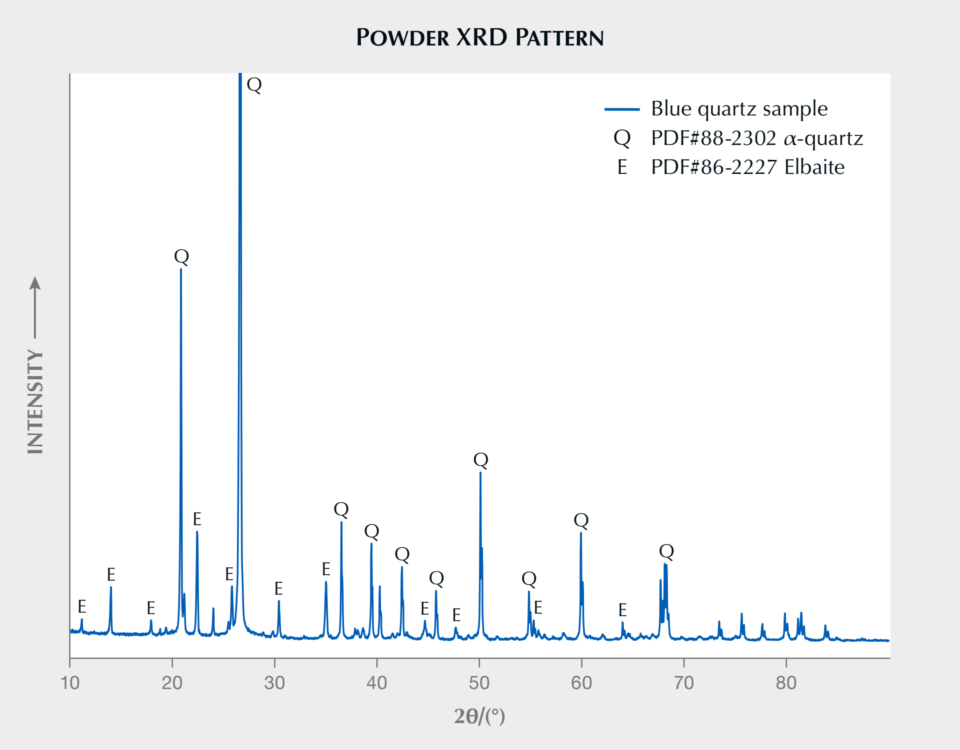

Figure 15. Powder XRD pattern of the 4.85 ct quartz sample, displaying characteristic peaks of α-quartz and elbaite.

luster of the quartz matrix. Semitransparent zones of the samples maintained full brightness in cross-polarized illumination while being rotated 360° in all directions, whereas the inclusion-dense areas remained opaque. Due to the optical behavior being obscured by numerous inclusions, thin sections were prepared from inclusion-rich areas of all three samples. Both the residual bulk material and the thin sections were subsequently examined by a combination of analyses, including polarizing microscopy, Raman spectroscopy, FTIR, laser-induced breakdown spectroscopy (LIBS), energy-dispersive X-ray fluorescence (EDXRF), and X-ray diffraction (XRD).

In cross-polarized light, the entire quartz host went extinct at the same time, confirming the quartz was a single crystal. In the thin section from the left sphere in figure 13, seven voids (0.3 to 0.6 mm in diameter) and three fractures (0.01 to 0.04 mm in width) were observed within the quartz matrix. Some of these voids were filled with acicular minerals (figure 14). This sample's lower SG of 2.50 compared to quartz's theoretical value is likely attributed to these voids and fractures. Under plane-polarized light, the blue acicular inclusions displayed strong pleochroism, transitioning from deep blue to pale blue.

Raman spectroscopy of the inclusions detected peaks at 225, 267, 370, 640, and 707 cm^{-1}, consistent with elbaite (R100137) in the RRUFF database (B. Lafuente et al., 2015, https://rruff.info/about/downloads/HMC1-30.pdf). XRD also identified their mineralogical phase as elbaite, revealing that one specimen (figure 13, top, left stone) exhibited an elbaite content of approximately 20 wt.% (figure 15). Since black tourmaline is a common type of inclusion in quartz, this case of blue elbaite inclusions responsible for the blue bodycolor in these quartz samples is rare.

LIBS identified lithium, sodium, magnesium, calcium, aluminum, silicon, iron, and boron in these inclusions (figure 16). The LIBS and EDXRF analyses detected iron but not copper or manganese, suggesting that the blue color was primarily attributable to iron, potentially by an Fe^{3+}-Fe^{2+} intervalence charge transfer.

FTIR revealed organic absorption peaks at 3036, 3057, 2958, 2928, and 2870 cm^{-1}. Raman peaks at 639, 1110, 1184, and 1605 cm^{-1} confirmed the presence of epoxy resin in the fractures and voids, indicating resin infiltration for structural stabilization and to improve transparency.

The systematic differentiation of single-crystal versus polycrystalline aggregates is critical to gemological classification. This is one case study in which sample morphology or inclusion density complicates identification, but thin section polarized microscopy observation and related analyses provided simple yet effective methods for determining the mineral phases.

Rong Liang, Ying Ma, Huihuang Li,
Rongxiang Du, and Muyu Chen
National Gemstone Testing Center
Shenzhen, China

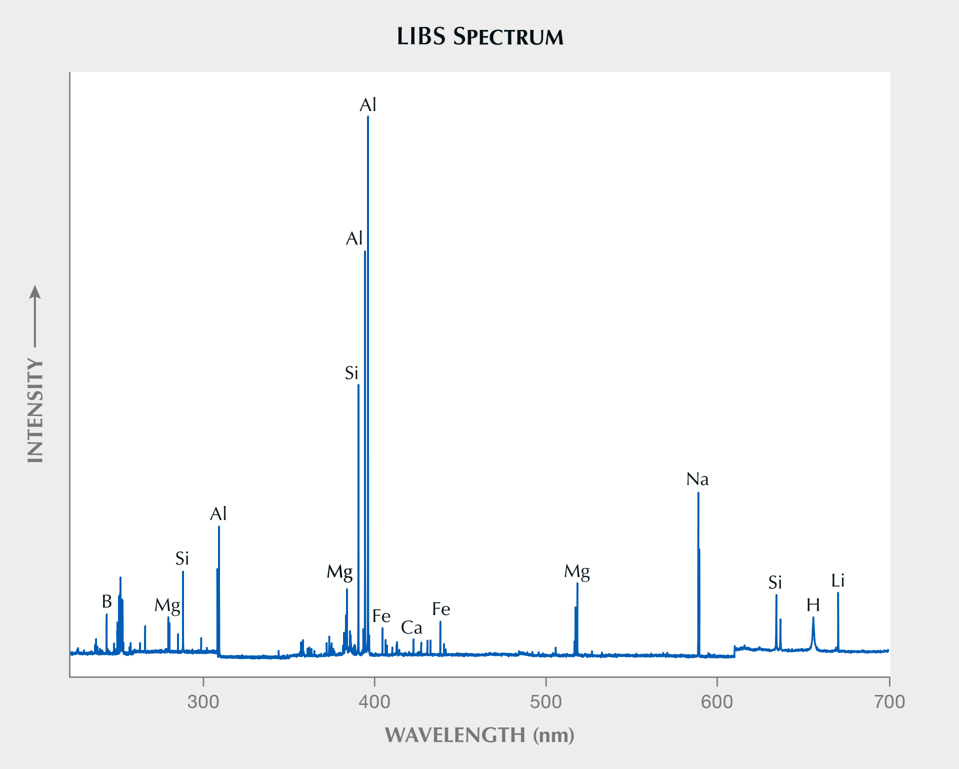

Figure 16. LIBS spectrum of an elbaite inclusion in the 5.50 ct quartz sample using a 266 nm laser showed characteristic emission lines of boron, magnesium, silicon, aluminum, iron, calcium, sodium, hydrogen, and lithium.

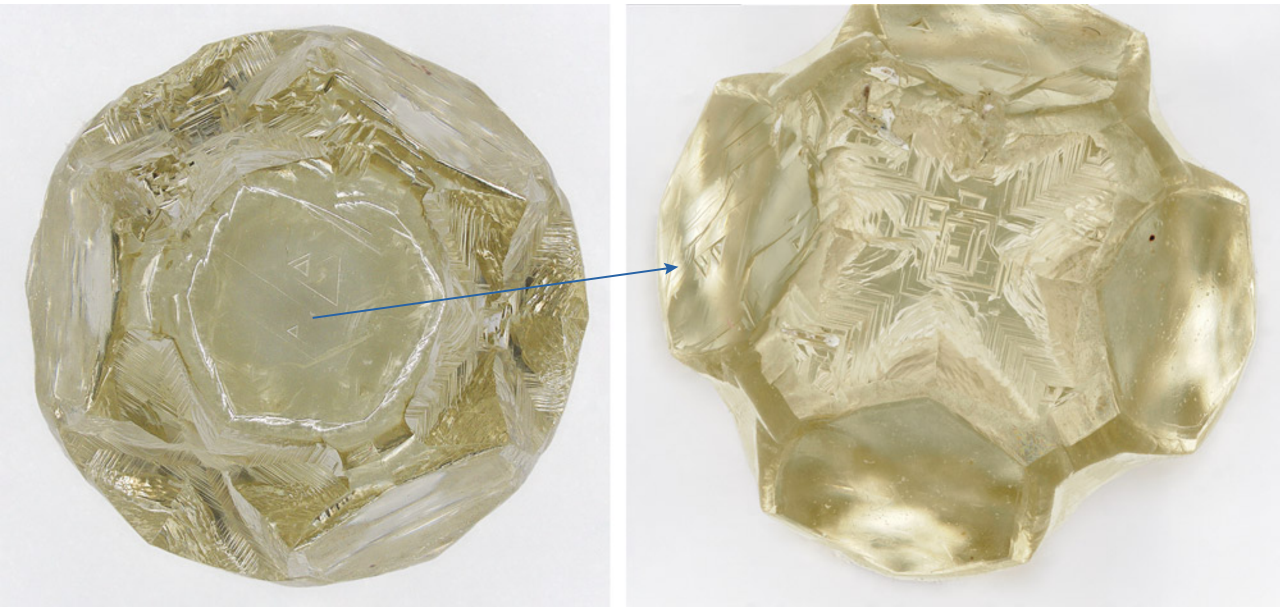

Figure 17. Left: This 3.49 ct yellow diamond with a diameter of ~7 mm exhibits a unique shape due to a combination of growth and dissolution features. Right: Tetragonal etch pits suggesting dissolution on cubic faces of initial habit. Photos by Cristiano Ferraris.

DIAMONDS

Unusual yellow diamond with a complex growth history. A rare yellow 3.49 ct diamond from a private collector exhibiting an unusual form due to a combination of growth and dissolution features was recently studied by the authors (figure 17). Microscopic examination highlighted the absence of solid inclusions and the presence of brown stains near the surface (figure 18, left). The stains were due to natural irradiation causing the formation of GR1 defects, implying that the stains were initially green and turned brown after the annealing process (S. Eaton-Magaña et al., "Low-temperature annealing and kinetics of radiation stains in natural diamond," *Diamond and Related Materials*, Vol. 132, 2023, article no. 109649).

Ultraviolet/visible/near-infrared spectroscopy indicated absorption features at 415, 373, 383, 392, and 404 nm related to N3 and N2 defects. A small percentage of yellow diamonds with these defects also contain hydrogen-related defects (C.M. Breeding et al., "Natural-color green diamonds: A beautiful conundrum," Spring 2018 *G&G*, pp. 2–27). In fact, the infrared spectrum of this stone showed the absorption peaks at 3107 and 1405 cm^{-1} characteristic of N_3VH^0 defects. With the sharp 3107 cm^{-1} peak, the hydrogen concentration was enough to classify the diamond as "hydrogen-rich" (T. Hainschwang et al., "A defect

Figure 18. Brown stains near the surface (left) and a trigon on the octahedral face (right) of the diamond. Photomicrographs by Cristiano Ferraris; fields of view 2.43 mm (left) and 1.82 mm (right).

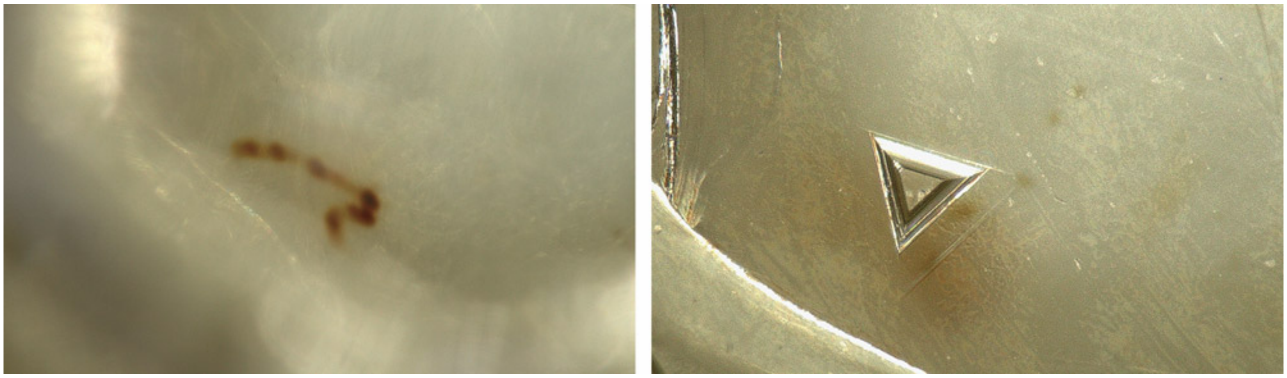

study and classification of brown diamonds with non-deformation-related color," *Minerals*, Vol. 10, No. 10, 2020, article no. 914). The peak at 1377 cm^{-1} indicated that the diamond also contained platelets (i.e., extended planar defects considered byproducts of nitrogen aggregation) (J.P. Goss et al., "Extended defects in diamond: The interstitial platelet," *Physical Review B*, Vol. 67, No. 16, 2003, article no. 165208).

While its color and size were impressive, the unique shape of the diamond, a result of growth and dissolution events, attests to the specimen's complex history. The yellow diamond's well-developed octahedral faces were marked by the presence of shallow trigons (figure 18, right) and separated by slightly curved resorbed faces. Tetragonal etch pits were clearly recognizable in this diamond (figure 17, right). This type of pit has been observed in diamonds from Botswana (C.M. Welbourn et al., "A study of diamonds of cube and cube-related shape from the Jwaneng mine," *Journal of Crystal Growth*, Vol. 94, No. 1, 1989, pp. 229–252) and are referred to as "re-entrant cubes," indicating dissolution processes that modified the initial cuboctahedral mixed habit. Unfortunately, the geological and geographical provenances of the yellow diamond are unknown, making the reconstruction of the formation conditions more difficult. However, trigon features (such as size and shape) can provide information about fluid composition and temperature during dissolution event(s) (Y. Fedortchouk et al., "Diamond destruction and growth during mantle metasomatism: An experimental study of diamond resorption features," *Earth and Planetary Science Letters*, Vol. 506, 2019, pp. 493–506), helping to determine if this occurred during kimberlite transport or mantle storage (K.V. Smit and S.B. Shirey, "Diamonds are not forever! Diamond dissolution," Spring 2020 *G&G*, pp. 148–155). A possible formation history of this exceptional diamond has been recently proposed by authors IP and CF (I. Pignatelli and C. Ferraris, "A rare yellow diamond: Reconstruction of the possible geological history," *Crystals*, Vol. 15, No. 5, 2025, article no. 461) on the basis of non-destructive analyses.

Isabella Pignatelli
Université de Lorraine, Centre de Recherches
Pétrographiques et Géochimiques (CRPG)
Nancy, France

Cristiano Ferraris
Institut de Minéralogie,
de Physique des Matériaux et de Cosmochimie,
Museum National d'Histoire Naturelle
Paris, France

Dominik Schaniel
Université de Lorraine, CNRS,
Laboratoire de Cristallographie,
Résonance Magnétique et Modélisation
Nancy, France

Diamond ring prize from an arcade-style claw game. In Tokyo, the author recently had the opportunity to play a coin-operated claw game (figure 19A) for 100 yen (approximately US$0.70). The prizes offered were gold-colored rings set with natural diamond, cubic zirconia, or white topaz. After 24 attempts, the ring shown in figure 19 (C and D) was captured. The label on the box noted the following:

Figure 19. A: The arcade-style claw game. B: The diamond ring prize packaged in a paper box. C and D: The diamond ring shown from two angles: front view and back view. Photos by Mari Sasaki (A) and Shunsuke Nagai (B–D).

adjustable-size brass ring with 18K gold plating, natural diamond of approximately 0.01 ct, made in Japan, along with the names of the manufacturer and distributor (figure 19B).

The ring itself, weighing 1.28 g, had a simple open-band design, with a diameter of about 18 mm and a width ranging from 5.6 to 2.4 mm. For closer inspection, the stone was removed, which damaged the ring's prongs and surrounding areas of metal. The small melee stone weighed 0.0119 ct—consistent with the "approximately 0.01 ct" packaging claim—and measured around 1.37–1.38 mm in diameter and 0.88 mm in depth (figure 20). Internal fractures were observed in the brownish orange-yellow stone, which exhibited poor clarity. The crown featured a table surrounded by eight facets, while the pavilion also displayed eight facets, suggesting a single-cut stone, with visible chips on the girdle and culet.

Standard gemological testing, including photoluminescence and ultraviolet/visible spectroscopy, confirmed that the stone was indeed a natural untreated diamond. Energy dispersive X-ray fluorescence spectroscopy revealed that the metal was a gold-plated alloy of copper, zinc, and nickel, matching the gold-plated brass description on the package.

Interestingly, the promotional poster inside the machine described the diamonds as "transparent" and "colorless," which was clearly not the case with this ring. The tested sample featured on the poster may have been colorless, but colored diamonds could have been mixed in during mass production. Japanese regulations limit the market value of claw machine prizes to around 1,000 yen (approximately US$7) (Summer 2024 GNI, pp. 256–257), making it impossible for each prize to include a gem report confirming its features.

In a previous attempt with another machine, the author won a 0.06 ct "yellow diamond" for about 800 yen (approximately US$5.60). Testing indicated it was a treated, artificially irradiated, natural brownish greenish yellow diamond. Though a prize may be labeled simply as "diamond," considering the possibility of treatments is advised.

Mari Sasaki
GIA, Tokyo

Figure 20. Table (left) and pavilion (right) views of the removed 0.0119 ct melee stone. Photos by Shunsuke Nagai.

TREATMENTS

Low-temperature heat treatment of corundum and the behavior of the 3161 cm^{-1} infrared band. The 3161 cm^{-1} infrared (IR) band can be observed in variously colored natural corundum, most commonly in yellow sapphire. The presence of this feature is used frequently as supporting evidence to conclude that a sapphire has not been heat treated (C.M. Breeding and N.J. Ahline, "Infrared spectroscopy and its use in gemology," Winter 2024 *G&G*, pp. 474–492). This 3161 cm^{-1} band is often present with other less intense side bands known as the "3161 cm^{-1} series" and includes features at ~3355, 3242, 3100 (shoulder), 2460, and 2420 cm^{-1} (C.P. Smith and C. van der Bogert, "Infrared spectra of gem corundum," Fall 2006 *G&G*, pp. 92–93). The exact origin of the 3161 cm^{-1} band is not well understood, although it is thought to be related to stretching vibrations of hydroxyl groups caused by interstitial H$^+$ ions present as charge compensation for Fe^{2+} substituting for Al^{3+} in the corundum structure (M.C. Jollands et al., "Vibrational properties of OH groups associated with divalent cations in corundum (α-Al$_2$O$_3$)," *European Journal of Mineralogy*, Vol. 35, No. 5, 2023, pp. 873–890).

As previously reported by Atikarnsakul and Emmett (Fall 2021 GNI, pp. 286–288), the intensity of the 3161 cm^{-1} band does not change after heating at 700°C in air, but it disappears or significantly decreases in intensity after heating at 900°C and above. Additionally, the prominent broad band at around 3000 cm^{-1} together with the 2625 cm^{-1} band, or the so-called "3000 cm^{-1} band series," can be created in some heated yellow sapphires containing low iron concentrations after heating at 900°C and higher. This series is related to stretching modes of hydroxyl groups in corundum doped with Mg^{2+} (N. Fukatsu et al., "Incorporation of hydrogen into magnesium-doped α-alumina," *Solid State Ionics*, Vol. 162–163, 2003, pp. 147–159). The 3000 cm^{-1} band series can also be observed in high iron yellow sapphires from basalt-related deposits without artificial heat treatment (Fall 2016 GNI, pp. 325–327). Moreover, a combination of the 3161 cm^{-1} series and the 3000 cm^{-1} series has been

Figure 21. Color-calibrated photos of studied natural corundum crystals from various deposits ranging from 0.44 to 1.28 ct before (left) and after heating at 850°C (right). At this heating temperature, stronger yellow/orange coloration can be created. Photos by Sasithorn Engniwat.

reported in a few untreated Rock Creek sapphires from the state of Montana (J.L. Emmett et al., "Yellow sapphire: Natural, heat-treated, beryllium-diffused, and synthetic," Fall 2023 *G&G*, pp. 268–297).

In this study, 10 natural corundum samples of various colors from GIA's colored stone reference collection were selected to analyze the thermal behavior of the 3161 cm^{-1} IR feature starting with its strong intensity prior to any heating (figure 21). These untreated stones were from various deposits: Madagascar (samples C1, C2, C5, C6, and C7), Myanmar (sample C3), Sri Lanka (samples C4 and C8), and Mozambique (samples C9 and C10). The stones were heated in air to 650°, 700°, 750°, 800°, 850°, and 900°C for 5 hours at each temperature. At the end of each heating session, the samples were rapidly cooled to room temperature, and color-calibrated photos and Fourier-transform infrared absorption (FTIR) spectra were collected. The light yellow zones exhibited a stronger yellow color after heating at 800°–850°C (samples C1 to C8). Additionally, when present, blue color zones became less saturated after heating at 800°C (samples C7 and C8).

For comparison, unpolarized FTIR spectra were recorded at the identical sample area after heating at each experimental temperature. Figure 22 shows FTIR spectra of sample C1 before heating and after heating at 750°, 800°,

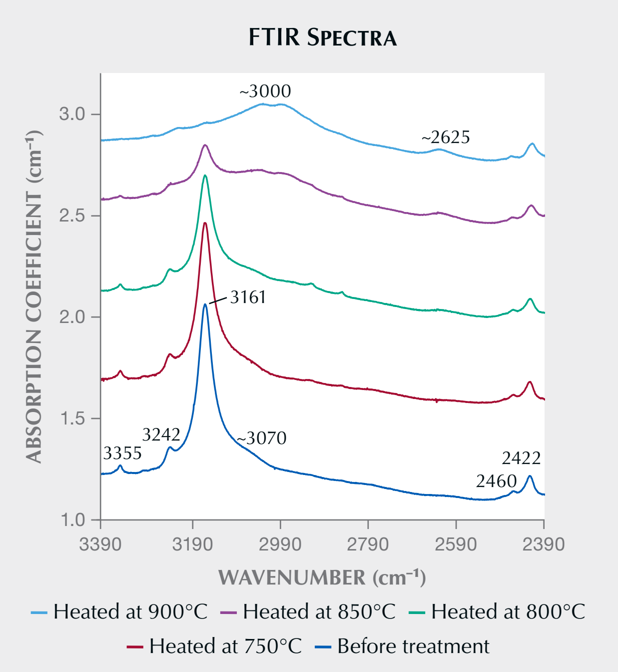

Figure 22. FTIR spectra of sample C1 before heat treatment and then heated at 750°, 800°, 850°, and 900°C for 5 hours at each temperature. After heating at 850°C, both the 3161 cm^{-1} series and the 3000 cm^{-1} band series were present in the same spectrum. Spectra are offset vertically for clarity.

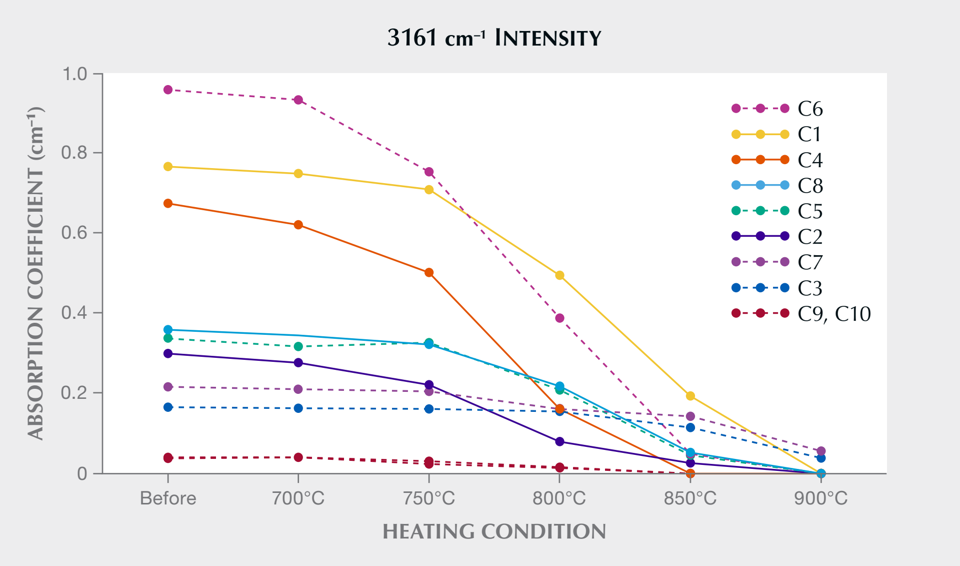

Figure 23. Variation in the 3161 cm^{-1} IR band intensity of the samples with no treatment and after 5 hours of heat treatment at 700°, 750°, 800°, 850°, and 900°C. Solid lines represent the samples that produced the 3000 cm^{-1} band after heat treatment, and dashed lines show those that did not produce any features after heat treatment.

850°, and 900°C. An insignificant to slight decrease in the 3161 cm^{-1} band intensity was observed after heating at 750°C or lower (figure 23). When heating between 800° and 850°C, the 3161 cm^{-1} intensity reduced significantly in all samples (figure 23), and the 3000 cm^{-1} band series was created in some samples, resulting in a combination of the 3161 cm^{-1} and the 3000 cm^{-1} band in the same spectrum (figure 22, purple line). After heating at 900°C, the 3161 cm^{-1} band either disappeared entirely or was still present but at a much lower intensity.

These experimental results and the previous work cited above indicate that natural corundum from different deposits possibly formed under various growth conditions such as temperature. Geological origin should also be taken into consideration when using the 3161 cm^{-1} and/or the 3000 cm^{-1} IR band to identify the presence of heat treatment.

Wasura Soonthorntantikul
GIA, Bangkok

Aaron C. Palke
GIA, Carlsbad

ERRATUM

In the Summer 2025 Colored Stones Unearthed section titled "Gem Granitic Pegmatites," a citation was incorrectly omitted on p. 192. In the second column, the first full paragraph should begin with "According to London (2008, p. 4), the name *pegmatite*…." We apologize for this error.